ResearchGate

See discussions, stats, and author profiles for this publication at: https://www.researchgate.net/publication/273000214

A multiscale study of inherent anisotropy and strain localization in granular soils

CONFERENCE PAPER · JANUARY 2015

DOI: 10.3208/jgssp.TC105-02

READS

109

3 AUTHORS:

Jidong Zhao

The Hong Kong University of Science and T…

72 PUBLICATIONS **571** CITATIONS

SEE PROFILE

Ning Guo

The Hong Kong University of Science and T…

20 PUBLICATIONS **145** CITATIONS

SEE PROFILE

Waiching Sun

Columbia University

42 PUBLICATIONS **210** CITATIONS

SEE PROFILE

Available from: Waiching Sun
Retrieved on: 19 March 2016

A multiscale study of inherent anisotropy and strain localization in granular soils

Jidong Zhao [i)], Ning Guo [ii)] and WaiChing Sun [iii)]

i) Associate Professor, Department of Civil and Environmental Engineering, Hong Kong University of Science and Technology, Clearwater Bay, Kowloon, Hong Kong.
ii) Postdoc Fellow, Department of Civil and Environmental Engineering, Hong Kong University of Science and Technology, Clearwater Bay, Kowloon, Hong Kong.
iii) Assistant Professor, Department of Civil Engineering and Engineering Mechanics, Columbia University, 500 West 120th Street, New York, NY 10027, USA.

ABSTRACT

This paper presents a multiscale study on inherent anisotropy and strain localization in granular soils. We employ a newly developed hierarchical framework coupling FEM and DEM. The framework features a hierarchical coupling scheme to solve a boundary value problem by FEM while deriving the constitutive relation required at each FEM Gauss point from the DEM solution of the embedded representative volume element. It helps circumvent the need for phenomenological constitutive assumptions and provides direct correlation between macroscopic observations and microscopic mechanisms. The study employs elongated particles for the local DEM packings to simulate inherent anisotropy in sand. By varying bedding plane angles (particle orientations), specimens with different inherent anisotropies are generated and are then sheared with smooth loading platens under drained biaxial conditions. A strong correlation is found between inherent anisotropy and strain localization, and fabric evolution underpins the final pattern of shear band since both type-a and type-b shear bands are observed in the simulations. In particular, non-coaxiality is identified as a direct attributor to break symmetry and trigger strain localization in a sample, while the formation process of shear band hinges crucially on the interplay between two sources of fabric anisotropy, particle orientation based and contact normal based. Fabric anisotropy of the former source is more difficult to mobilize than that of the latter. Cross-scale analyses indicate the DEM packings inside the shear band undergo extensive shearing, fabric evolution and particle rotation and may reach the critical state, while those located outside the shear band may experience unloading.

Keywords: multiscale modeling, inherent anisotropy, strain localization, fabric evolution, non-coaxiality

1. INTRODUCTION

Anisotropy is found a key factor affecting the occurrence of strain localization in granular soils, among many others such as density, drainage conditions, boundary conditions and specimen dimension (Tatsuoka et al., 1990; Vardoulakis, 1996; Desrues and Viggiani, 2004; Lade et al., 2008). Continuum modelling based on finite element method (FEM) has been a popular tool in simulating strain localization in anisotropic soils as a boundary value problem (BVP) (Bauer et al., 2004; Tejchman et al., 2007; Gao and Zhao, 2013, 2014; Sun et al., 2014). There are also micromechanics-based studies, using DEM, on the modelling of shear band (e.g., Fu and Dafalias, 2011; Sun et al. 2013). The continuum approaches commonly need phenomenological assumptions on the constitutive relations, whereas the DEM-based approaches can rarely be applied to solve a BVP of engineering scale. We employ a novel hierarchical multiscale approach in this study to overcome the issues related to both methods. This multiscale modelling method was recently developed by the authors (Guo & Zhao, 2013a, 2014) in line with the concept presented by Nitka et al. (2011) and Andrade et al. (2011). As illustrated in Fig. 1, the computational multiscale framework treats the problem domain as a continuum and discretises it by finite element mesh. At each Gauss point of the FEM mesh, instead of using a presumed constitutive model, a separate DEM test is performed to provide the local material response required for the FEM integration. Each DEM packing hence serves as a representative volume element (RVE) to derive the material constitutive relation, and to circumvent the phenomenological assumptions and parameter fitting in conventional continuum approaches. The multiscale approach expedites a direct link of macroscopic soil

behavior with its microscopic origin, and hence helps to gain micromechanical insights into complex soil properties such as history-dependency, non-coaxiality, state-dependent dilatancy and the critical state, as well as anisotropy and strain localization to be considered in the following. Details of the formulation and solution can be referred to Guo & Zhao (2014).

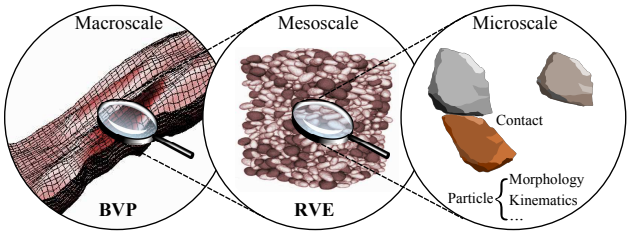

Fig. 1. Illustration of the hierarchically coupled FEM-DEM multiscale modeling framework.

2 GENERAL SPECIFICATIONS

2.1 DEM model and anisotropic RVEs

To simulate inherent anisotropy, elongated clumps consisting of two identical disks as shown in Fig. 2 are used in the DEM packing. The two clumped circular disks have a centroid distance of $1.25r$ (r = the radius of the constituent disks), which leads to a clump of aspect ratio at 1.625. A linear contact similar to Guo & Zhao (2014) is employed using a normal stiffness $k_n/r_{eq} = 455$ MPa and the tangential stiffness $k_t = 0.3\ k_n$ (r_{eq} = the common radius of the two contacting particles). The Coulomb friction law is used to describe the interparticle friction with an interparticle frictional angle $\psi = 0.5$ rad. The density of clumps is set to be $\rho_{cl} = 2650$ kg/m^3.

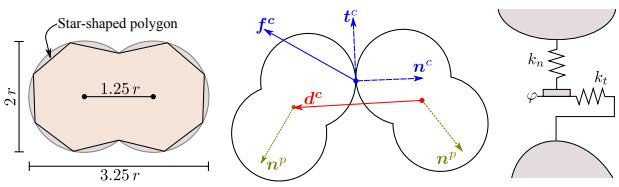

Fig. 2. Clumped particles used in the DEM simulation.

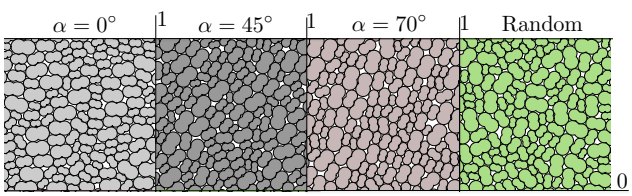

Fig. 3. Anisotropic RVE packings generated for the study.

A DEM assembly containing 400 clumps with equivalent radius raning from 3 mm to 7 mm is used for the RVE. 2D case is considered in the study, so all particles are assumed to have a thickness of 100 mm (e.g., 10 times of the mean particle diameter). To prepare RVEs with different inherent anisotropies, five RVE packings with bedding plane angle relevant to the horizontal as shown in Fig. 3, α = 0°, 22.5°, 45°, 70° and randomly orientated, are prepared. Periodic boundary conditions are imposed on each RVE assembly in the subsequent multiscale simulations.

2.2 Homogenized macro quantities

The Cauchy stress tensor and the tangent modulus, which are crucial to the multiscale computation, can be homogenized from the DEM packing at each Gauss point, according to:

$$\sigma_{ij} = \frac{1}{V}\sum_{c\in N_c} d_i^c f_j^c \tag{1}$$

$$D_{ijkl} = \frac{1}{V}\sum_{c\in N_c}\left(k_n n_i^c d_j^c n_k^c d_l^c + k_t t_i^c d_j^c t_k^c d_l^c\right) \tag{2}$$

where V is the total volume of the assembly. N_c is the total contact number. $\mathbf{n}^c$ is the unit outer normal of a contact. $\mathbf{d}^c$ is the branch vector. $\mathbf{t}^c$ is the unit vector along the tangential direction of a contact. $\mathbf{f}^c$ is the interparticle contact force.

Key to the present study is the comparison of two sources of fabric anisotropy in the initiation and development of strain localization, namely, one being particle orientation based and the other related to the contact normal, which are respectively defined as follows:

$$\phi_{ij}^I = \int_\Theta E(\Theta) n_i^I n_j^I \, d\Theta = \frac{1}{N_I}\sum_{c\in N_I} n_i^I n_j^I \qquad (I = p, c) \tag{3}$$

where $I = p$ and c denote respectively the particle orientation based and contact normal based definitions. $E(\Theta)$ is the distribution density function of either the particle orientation vector or the contact normal vector. In practice it is convenient to use the deviatoric tensor of the fabric tensor in Eq. (3) for discussion, e.g., $F_{ij}^I = 4\left(\phi_{ij}^I - \delta_{ij}/2\right)$ for a 2D case (δ_{ij} = Kronecker delta). A scalar F_I can be used to measure the anisotropic intensity: $F_I = \sqrt{F_{ij}^I F_{ij}^I / 2}$.

2.3 RVE responses

Figure 4 presents the homogenized responses of the five RVEs under drained biaxial compression. The RVE responses are generally consistent with laboratory observations on sand samples. The peak stress of the RVE decreases steadily with the increase of the bedding plane angle. The α = 0° RVE packing shows the most dilative response accompanied with a drastic post-peak softening behavior in terms of stress, whereas the dilation and the softening for the α = 70° RVE packing are relatively mild. The random packing gives rise to an intermediate strength and dilation behavior among all the RVEs. The peak principal stress ratio varies from 6.5 to 4.1 for the five cases, with the final stage dilation varying from -6.6% to -4.9%. Note that in Guo & Zhao (2014) where circular particles were used,

the peak stress ratio of the RVE can only reach about 2.8 with a dilation of around -3.8% at the same shearing level. Clearly, the use of clumped particles yields a much higher strength and a more dilative response for the RVE packing, which is attributable to particle interlocking.

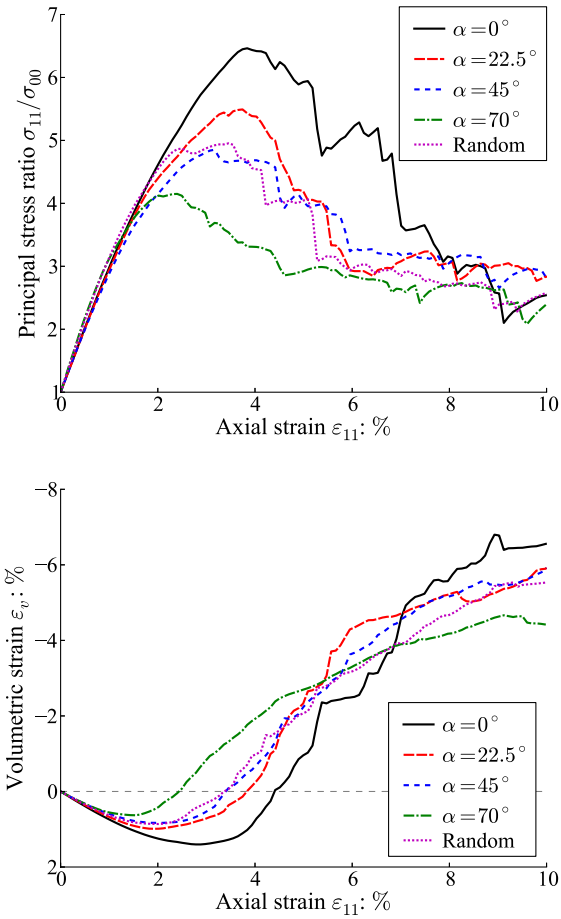

Fig. 4. RVE responses under drained biaxial compression (top: stress-strain relation; bottom: dilation curve).

3 MULTISCALE MODELING OF BIAXIAL SHEAR ON SAND

3.1 Model setup and global sample responses

A specimen of 50 mm by 100 mm in dimension is discretized into 8-node quadrilateral elements as shown in Fig. 5. The top platen is smooth. A reduced integration scheme using 2×2 Gauss points is adopted. The specimen is initially uniform by assigning identical RVEs to all Gauss points. It is first isotropically consolidated to a target initial mean effective pressure σ_{00} = 100 kPa. Compression is then applied along the vertical direction, while the horizontal confining pressure is kept constant at σ_{00} = 100 kPa. Figure 6 provides the resultant global axial stresses exerted on the top surfaces of the five specimens. A consistent general trend with the RVEs is that the peak stress decreases with the increase of bedding angle, while the post-peak stress reduction in the multiscale simulation is more dramatic than that in RVE element test due to the formation of shear band in the BVP. Fig. 6 also shows a marginal difference between the results (denoted by open circles) by a full integration scheme for finite element (e.g., 3 by 3) with those obtained by the reduced scheme (solid line), which indicates that the high-order 8-node element with reduced integration is accurate enough while being computationally efficient.

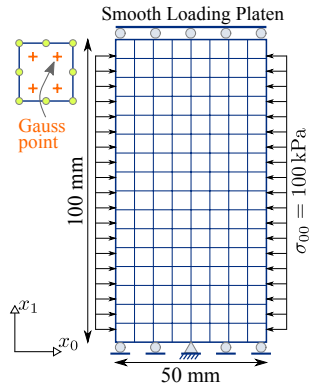

Fig. 5. Multiscale model setup for a sand sample under constant pressure biaxial shear with smooth loading paten.

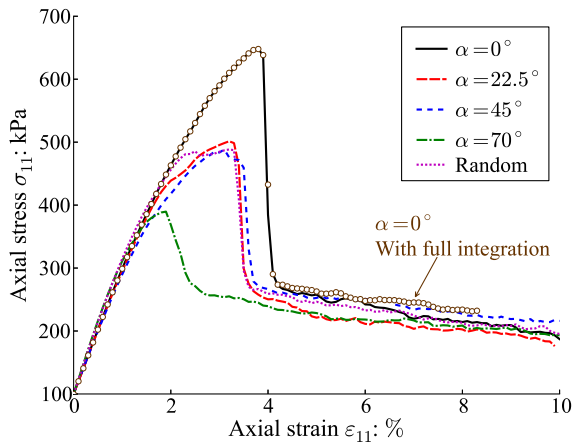

Fig. 6. Multiscale model setup for a sand sample under constant pressure biaxial shear with smooth loading paten.

3.2 Strain localization and shear banding pattern

Figure 7 shows the contours of the accumulated deviatoric strain and void ratio for two sample cases at the peak stress state and the final state, respectively. Apparently, strain localization occurs in both cases. For the α = 22.5° case at the peak stress state, the sample is relatively homogeneously deformed, with ε_q ranging from 5.75% to 5.94% and e ranging from 0.123 to 0.124. However, for the α = 45° case at the peak stress state, the contours of ε_q and e both show a relatively broader variation. This suggests the localization has developed to a certain extent at the peak for this case, and as a result, a smaller global peak stress is observed compared with the RVE element test. Intense localization and apparent shear bands can be more easily identifiable towards the final loading stage in

both samples. At ε_{11} =10%, the accumulated deviatoric strain may reach 172%~198% within the localized region in the two samples. The patterns (in terms of inclination and position) of the final shear bands are persistent to their incipient forms at the early peak stress states. Notably, the minimum ε_q at the final state is even smaller than that in the peak stress state in both cases. This is because some regions outside the localized area experience unloading during the post-peak softening stage when more deformation is localized inside the shear band. Meanwhile, the localized shear band also corresponds to the most dilative area with largest void ratios, which is consistent with experimental observations.

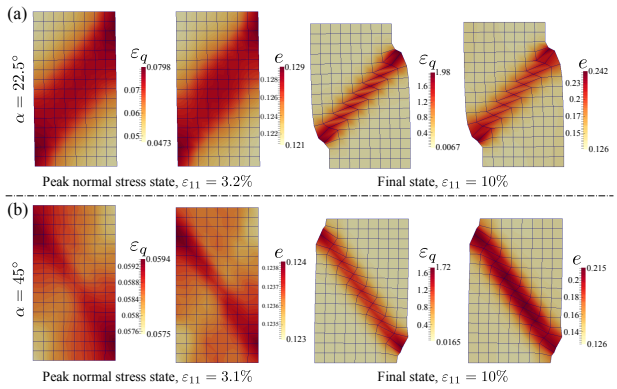

Fig. 7. Contours of the accumulated deviatoric strain and the void ratio for (a) the α = 22.5° and (b) the α = 45° specimens at different shearing levels. Note that the color bars in the legends are in different ranges.

3.3 Fabric evolution and particle rotation

Fig. 8 presents the particle orientation based fabric anisotropy F_p and the average particle rotation defined below for the α = 22.5° case and the random case:

$$\bar{\theta} = \frac{1}{N_p} \sum_{c \in N_p} \theta^p \tag{4}$$

where θ^p is the accumulated rotation of an individual particle (anti-clockwise rotation is taken as positive). Evidently, the contours both F_p and $\bar{\theta}$ show similar patterns with the shear strain and void ratio in Fig. 7. The particles inside the shear band rotate apparently more substantially than those outside, which is consistent with both laboratory experiments (Hall et al., 2010) and pure DEM simulations (Bardet and Proubet, 1991). Also notably, $\bar{\theta}$ is anti-clockwise in the case of α = 22.5° and is clockwise in the random case, which is apparently related to the totally different developing orientation of shear band in the two case. Interestingly, the F_p for the α = 22.5° case decreases inside the shear band with shearing and reaches a minimum compared to the outside regions, whereas it gradually increases within the shear band for the random case and reaches a maximum at the final state. Also shown in Fig. 8, the contours of both deviatoric stress q and the contact normal based fabric anisotropy F_c are found unsuitable to identify shear band (see also Guo and Zhao, 2014).

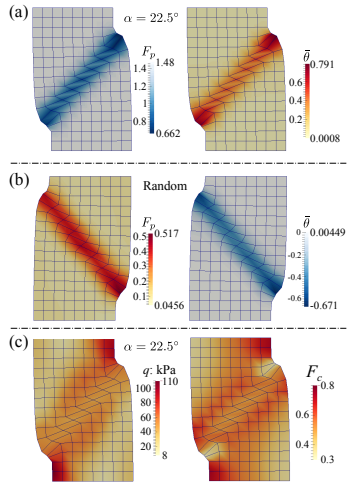

Fig. 8. Contours of F_p and $\bar{\theta}$ for (a) the α = 22.5° and (b) the random specimens at final stage. (c) contours of for q and F_c the α = 22.5° case.

It is interesting to observe in Fig. 7 that the orientations of shear band in the two specimens are totally different. In the case of α = 22.5° it inclines more closely to the bedding plane direction which is termed as a type-b shear band by Tatsuoka et al. (1990). The α = 45° specimen has a shear band pattern orientating more to the perpendicular direction of the bedding plane which is called by Tatsuoka et al. (1990) as type-a shear band. Tatsuoka et al. (1990) observed both types of shear band pattern in their plane strain laboratory tests with lubricated loading platen. The occurrence of these two types of shear band signifies different failure mechanisms of strain localization. Type-a shear band is typically governed by the Coulomb's failure condition, while type-b band is controlled by a zero-extension failure mechanism (Tatsuoka et al., 1990; Gao & Zhao 2013).

3.4 Non-coaxiality and shear band

All simulations in this paper have been based on initially homogeneous specimens with symmetric boundary condition under smooth loading conditions. In a conventional FEM analysis, such samples are expected to undergo homogeneous deformation throughout the shearing course without incurring any strain localization, due to lacking of necessary triggers or symmetry breakers to induce strain localization. Indeed, most past studies have practically introduced either imperfections or random fields for elements/material parameters as triggers to simulate the phenomenon of shear banding. Since strain localization occurs in both initially anisotropic samples and the random sample, inherent anisotropy is not the key attributor to strain localization in the considered cases here. Indeed, the non-coaxial response of a granular material can play a role of symmetry breaker to trigger

strain localization, which has been demonstrated by Gao and Zhao (2013) and Guo and Zhao (2014).

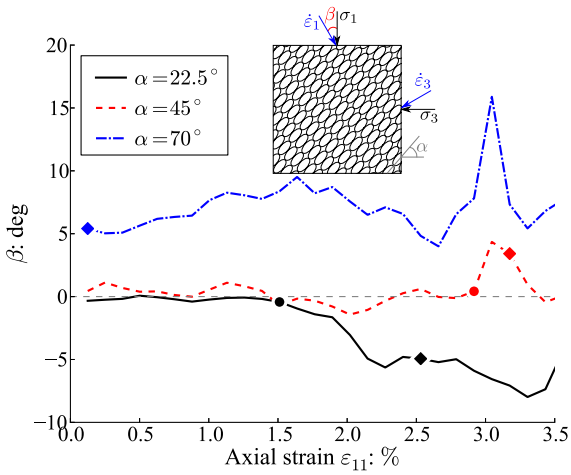

Fig. 9. Non-coaxial responses of the RVEs. The inset illustrates the definition of the non-coaxiality angle β.

Fig. 9 presents the responses of three RVEs based on their respective element tests under drained biaxial shear, where the non-coaxial behavior is evidently observable for each RVE. $\alpha = 22.5^{o}$ and $\alpha = 45^{o}$ RVEs depict a nearly coaxial response ($\beta = 0$) at the early shearing stage up to an axial strain about 2%-3%. After ε_{11} =1.55%, the $\alpha = 22.5^{o}$ RVE gradually develops a negative non-coaxiality, which triggers a type-b shear band as observed in Fig. 7, whilst the $\alpha = 45^{o}$ RVE develops a positive non-coaxiality leading to the formation of a type-a shear band. The $\alpha = 70^{o}$ RVE demonstrates a positive non-coaxial behavior from the beginning, which leads to a type-a shear band. Clearly, the non-coaxiality angle observed in the RVEs is not predetermined by the bedding plane orientation, but how the non-coaxiality is developed. The number of contact normals and the length of branch vectors defining the two fabric tensor in Eq. (3) can be identified as two major competing factors in determining non-coaxiality, since they directly influence the principal directions of the tangent modulus in Eq. (2) and hence governs the material non-coaxial response. Once the symmetry in deformation breaks down due to non-coaxiality, asymmetric displacement field will dominate the subsequent deformation of the sample.

3.5 Cross scale analysis

The hierarchical multiscale approach facilitates a direct correlation of the macroscopic observations with their underlying microstructural mechanisms through cross-scale analysis. Take the $\alpha = 0^{o}$ case as an example. Two typical Gauss points shown in Fig. 10e are selected for the analysis. Fig. 10 shows the material responses of both Gauss points extracted from their corresponding RVEs. Point A clearly exhibits a small deformation of loading followed by an unloading in which the loading path (Fig. 10b) is close to a perfectly drained one, indicating its stress almost returns to its initial isotropic state. In such a process, F_p at Point A stays almost unchanged, while F_c first undergoes a marked increase in loading and then decreases in unloading. The force chain network of the embedded RVE at Point A (Fig. 10d) is almost isotropic.

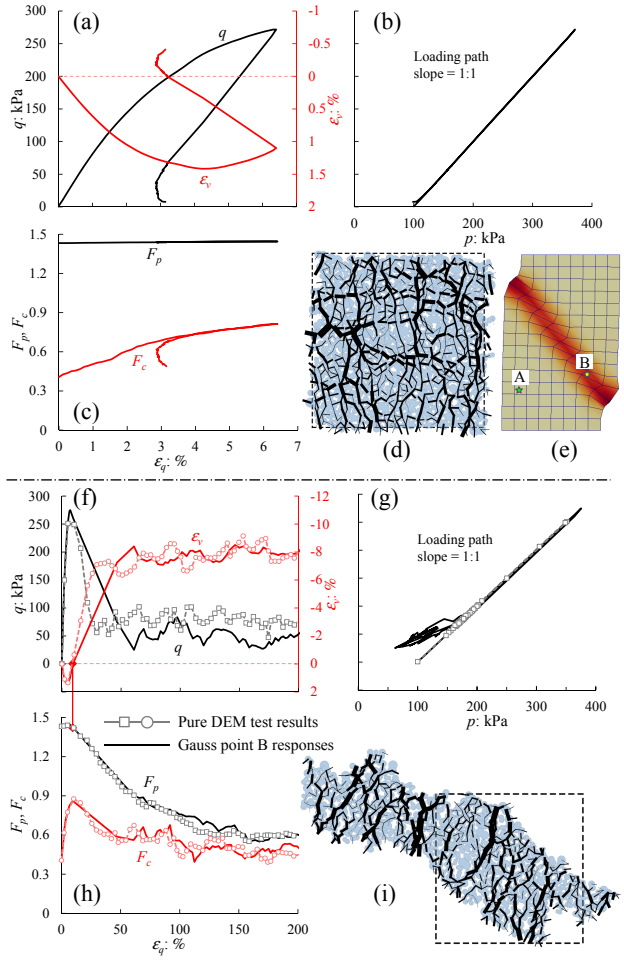

Fig. 10. Local Gauss points responses in the $\alpha = 0^{o}$ specimen: (a)-(c) Gauss point A responses; (d) RVE force chain of Gauss point A after shear; (e) locations of the two Gauss points in the deformed mesh; (f)-(h) Gauss point B responses; (i) RVE force chain of Gauss point B after shear.

Point B undergoes excessively large deformation, with its deviatoric stress increasing monotonically to around 200% before attaining critical state. The material responses at Point B appear to match the case of pure DEM results reasonably well. Both fabric anisotropies, F_p and F_c, at point B evolve significantly with shear strain. The zero volumetric strain point at a shear strain of around 9.5% can be regarded as a watershed point in observing their changes. F_c increases steadily upon shear, attains a peak of over twice of its initial value at the watershed point, and then drops gradually before reaching a critical state value. Prior to the watershed strain level, F_p shows marginally small increase only and then decreases steadily to a steady

critical value of around 40% of its peak value (see Guo and Zhao, 2013b and Zhao and Guo, 2013 for more discussion on critical fabric anisotropy). The final RVE at Point B is severely distorted with strong force chains penetrating the RVE.

In conjunction with the response of Point A, it suggests that the evolution of F_p is more difficult to mobilize than F_c. In addition to shearing, considerable dilation is required to allow the relaxation of interlocking and reorientation of particles to induce the change for F_p, which is in contrast to the immediate change of F_c upon shearing. The evolutions of the two fabric anisotropies are hence not synchronous, indicating a micromechanical mechanism accounting for the previous observations in Fig. 9 that an initially coaxial packing may develop substantial non-coaxiality at some small shearing levels. It also takes a significant shearing process for F_p to reach its critical state value (e.g., with a shear strain greater than 150% for Point B) that is hardly attainable in routine laboratory element tests. This explains why Wong and Arthur (1985) observed the survival of inherent anisotropy and limited particle orientation change in their tests.

4 CONCLUSIONS

The interplays between anisotropy and strain localization in granular soils were investigated using a novel hierarchical multiscale approach based on rigorous coupling of FEM and DEM. To model the presence of inherent anisotropy and its influence on the initiation and development of strain localization in sand, a simple clump model was introduced into the DEM part of the multiscale method and biaxial compression tests were carried out on samples under smooth boundary conditions. Through detailed analyses of the correlation between inherent anisotropy, fabric evolution, strain localization and non-coaxiality, the study sheds noel cross-scale insights into the understanding of strain localization and anisotropy which have long been considered two important phenomena for soil. Further study may consider using my realistic-shape particles (see, e.g., Mollon and Zhao, 2012, 2013, 2014) to replace the two-disk clumps to simulate anisotropy and strain localization.

ACKNOWLEDGEMENTS

The study was financially supported by Research Grants Council of Hong Kong (via RGC/GRF 623211).

REFERENCES

1) Andrade, J., Avila, C., Hall, S., Lenoir, N. and Viggiani, G. (2011): Multiscale modeling and characterization of granular matter: from grain kinematics to continuum mechanics, *J. Mech. Phys. Solids,* 59(2), 237-250.
2) Bardet, J. and Proubet, J. (1991): A numerical investigation of the structure of persistent shear bands in granular media, *Géotechnique,* 41(4), 599-613.
3) Bauer, E., Huang, W. and Wu, W. (2004): Investigations of shear banding in an anisotropic hypoplastic material, *Int. J. Solids Struct.*, 41(21), 5903-5919.
4) Desrues, J. and Viggiani, G. (2004): Strain localization in sand: an overview of the experimental results obtained in Grenoble using stereophotogrammetry, *Int. J. Numer. Analyt. Methods Geomech.*, 28(4), 279-321.
5) Fu, P. and Dafalias, Y. (2011): Fabric evolution within shear bands of granular materials and its relation to critical state theory, *Int. J. Numer. Analyt. Methods Geomech.*, 35(18), 1918-1948.
6) Gao, Z. and Zhao, J. (2013): Strain localization and fabric evolution in sand, *Int. J. Solids Struct.* 50(22-23), 3634-3648.
7) Gao, Z., Zhao, J., Li, X. & Dafalias, Y. (2014): A critical state sand plasticity model accounting for fabric evolution, *Int. J. Numer. Analyt. Methods Geomech.*, 38(4), 370-390.
8) Guo, N. and Zhao, J. (2013a): A hierarchical model for cross-scale simulation of granular media, *AIP Conference Proceedings*, 1542, 1222-1225.
9) Guo, N. and Zhao, J. (2013b): The signature of shear-induced anisotropy in granular media, *Comput. Geotech.*, 47, 1-15.
10) Guo, N. and Zhao, J. (2014): A coupled FEM/DEM approach for hierarchical multiscale modelling of granular media, *Int. J. Numer. Methods Engng*, 99(11), 789-818.
11) Hall, S. A., Bornert, M., Desrues, J., Pannier, Y., Lenoir, N., Viggiani, G. and Bésuelle, P. (2010): Discrete and continuum analysis of localised deformation in sand using X-ray μCT and volumetric digital image correlation, *Géotechnique*, 60(5), 315-322.
12) Lade, P., Nam, J. and Hong, W. (2008): Shear banding and cross-anisotropic behavior observed in laboratory sand tests with stress rotation, *Can. Geotech. J.*, 45(1), 74-84.
13) Mollon, G. and Zhao, J. (2012): Fourier-Voronoi-based generation of realistic samples for discrete modelling of granular materials, *Granular Matter*, 14(5), 621-638.
14) Mollon, G. and Zhao, J. (2013): Generating realistic 3D sand particles using Fourier descriptors, *Granular Matter*, 15(1), 95-108.
15) Mollon, G. and Zhao, J. (2014): 3D Generation of Realistic Granular Samples Based on Random Fields Theory and Fourier Shape Descriptors, *Comput. Methods Appl. Mech. Engng.*, 279, 46-65.
16) Nitka, M., Combe, G., Dascalu, C. and Desrues, J. (2011): Two-scale modeling of granular materials: a DEM-FEM approach, *Granular Matter*, 13, 277-281.
17) Sun, W., Kuhn, M. and Rudnicki, J. (2013): A multiscale DEM-LBM analysis on permeability evolutions inside a dilatant shear band. *Acta Geotechnica* 8(5), 465-480.
18) Sun, W., Ostien, J. and Salinger, A. (2014): Modeling the hydro-mechanical responses of strip and circular punch loadings on water-saturated collapsible geomaterials. *Acta Geotechnica* 9(5), 903-934.
19) Tatsuoka, F., Nakamura, S., Huang, C. and Tani, K. (1990): Strength anisotropy and shear band direction in plane strain tests of sand, *Soils Found.*, 30(1), 35-54.
20) Tejchman, J. and Górski, J. (2010): Finite element study of patterns of shear zones in granular bodies during plane strain compression, *Acta Geotech.*, 5(2), 95-112.
21) Vardoulakis, I. (1996): Deformation of water-saturated sand: I. Uniform undrained deformation and shear band, *Géotechnique*, 46(3), 441-456.
22) Wong, R. and Arthur, J. (1985): Induced and inherent anisotropy in sand, *Géotechnique*, 35(4), 471-481.
23) Zhao, J. and Guo, N. (2013): Unique critical state characteristics in granular media considering fabric anisotropy, *Géotechnique*, 63(8), 695-704.